Alma Mater Studiorum · Università di Bologna

Scuola di Scienze
Dipartimento di Fisica e Astronomia
Corso di Laurea in Fisica

Study of the performance of the prototype EIC dRICH readout based on SiPM with thermoelectric cooling

Relatore:
Prof.ssa Gilda Scioli

Correlatore:
Dott. Roberto Preghenella

Presentata da:
Matilde Zucchini

Anno Accademico 2021/2022

Sommario

L'Electron-Ion Collider è un futuro acceleratore di particelle che approfondirà la nostra conoscenza riguardo l'interazione forte tramite la collisione di elettroni con nuclei e protoni. Uno dei progetti attualmente considerati per la costruzione del rivelatore, il dual-radiator RICH, prevede l'impiego di due radiatori Cherenkov, sui quali verranno montati dei fotorivelatori per rilevare l'emissione della luce Cherenkov e risalire alla massa delle particelle. L'opzione di base per questi rivelatori sono i sensori al silicio SiPM.

Questo lavoro di tesi si basa sullo studio delle prestazioni di un prototipo per l'acquisizione dei dati rilevati dai SiPM che sfrutta l'effetto termoelettrico per raffreddare la zona in cui sono situati i sensori. L'analisi dei dati acquisiti ha portato alla conclusione che le prestazioni del prototipo sono confrontabili con quelle misurate all'interno di una camera climatica quando si trovano alla stessa temperatura.

Contents

Introduction

The Electron-Ion Collider is a future particle accelerator that will be built in the United States of America to study the strong interaction. The design currently under consideration for the detector, situated in the intersection regions of the accelerator consists in three major systems: tracking and vertexing, particle identification and calorimetry. The particle identification system includes a dual-radiator Ring Imaging Cherenkov (RICH) detector, which will involve the use silicon photomultipliers, a type of semiconductor photo detectors formed by an array of single photon avalanche diodes with a single photon detection capability.

The aim of this work is to compare the dark count rate of the SiPMs kept at a low temperature with a thermoelectric cooling system with the performance of the same sensors in a climatic chamber at the same temperature. The thermoelectric cooling system is based on the Peltier effect and will allow to cool only the desired area with no circulating fluids or moving parts.

Chapter 1 evolves around the Electron-Ion Collider, giving an overview of the scientific goals it aims to achieve and describing some of the designs currently taken under consideration.

Chapter 2 will give an overview of three of the main components of the experimental setup used in this study: silicon photomultipliers, Peltier modules and the ALCOR prototype ASIC for the SiPM readout. Each component will be analyzed both in operating principle and designs under consideration for this study.

In Chapter 3, the experimental setups will be presented, along with the measurements carried out to confront the dark count rate for sensors found at different temperatures and with different cooling systems.

Chapter 1

The Electron-Ion Collider

The Electron-Ion Collider (EIC) is a new particle accelerator that will be built in the next decade in the United States of America by the Department of Energy at Brookhaven National Laboratory (BNL). The EIC is designed to collide beams of polarized electrons with polarized beams of protons, polarized beams of light ions and beams of heavier ions (up to U) at high intensity. By using large detectors it will be able to obtain precise measurements that will allow physicists to have a better understanding of nuclear structure in terms of the fundamental quark and gluon constituents.

Gluons are the exchange particles for the strong force between quarks. Quarks and gluons, called collectively partons, are the fundamental constituents of nucleons and are studied in the Quantum Chromo-Dynamics (QCD) theory, that attributes the strong force between quarks and gluons to their color charge, which is also responsible of the interaction between gluons. This interaction generates a significant fraction of the nucleon mass leading to a regime of matter that can be studied when nucleons collide at high speeds. A deeper understanding of this regime will require the higher energy and beam polarization of the Electron-Ion Collider. Some of the questions the EIC will address include the origin of the nucleon mass and spin, the distribution of parton momenta and position inside the nucleon and the properties of a dense system of gluons. The versatile range of kinematic, beam polarization and beam species of the EIC will allow the study of all the subjects listed above in one facility. In the following sections, a summary of the main scientific goals as well as the accelerator design and detector requirements will be presented.

1.1 Scientific highlights

Here is a brief analysis of nucleon components EIC will take interest in, and how the specifics of this new particle accelerator will help investigate the role of partons in determining the nucleon properties [1].

Proton spin

The EIC is designed to facilitate the mapping of distribution of the nucleon momentum, including the transversal component, spin, flavor and partons. In particular, it is going to extend the knowledge on the role of gluons and sea quarks in determining the hadron structure and spin. The spin of quarks is responsible for only 30% of the proton spin. The spin of gluon, while it does contribute, cannot make up for the remaining 70%. The capability of the EIC to reach two orders of magnitude lower in the minimum momentum fraction x accessible by the experiment will lead to precisely quantify the contribution of the spin of quarks and gluons to that of the proton by colliding longitudinally polarized electron and nucleons.

Confined motion of partons

Inside a fast moving nucleon, the confined motion and spin of partons, as well as the spin of the nucleon, are correlated to transversal momentum dependent parton distributions (TMDs). These correlations can be traced back to the spin-orbit coupling among partons and, using electron and nucleon polarized beams, TMDs can reveal some new information about the motion of confined gluons and sea quarks.

Tomographic image of the proton

By probing the transversal spatial distribution of partons as a function of their longitudinal momentum fraction — that gives an image of the proton complementary to the one obtained from the transverse momentum distribution of partons — the EIC will be able to create a tomographic image of the proton, more precise on the transversal distances than any other existing facilities. This imaging technique contains information about spin-orbit correlations and about the angular momentum, spin and orbital motion of partons.

QCD matter at extreme gluon density

Gluon density is regulated by a non-linear process of gluon-gluon recombination, thus generating a dynamic saturation scale at which gluon splitting and recombination reach a balance. As they approach this scale, gluons should produce new properties in the hadrons. The saturation scale separates the condensed gluonic matter from the confined gluon and quarks in an hadron, as shown in Figure 1.1. By colliding heavy ion beams, the EIC could provide a saturation scale large enough to systematically compute the hadron properties that derive from the state of high gluon density.

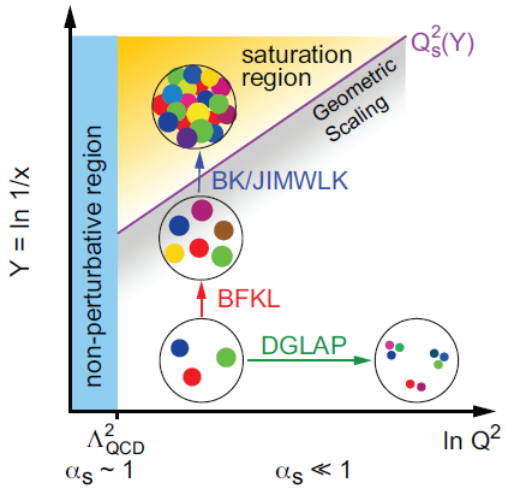

Figure 1.1: Schematic probe resolution vs. energy landscape. In the perturbative QCD region is shown from low to high the saturated parton density.

Quark hadronization

The EIC will also complement the investigation of the interaction between light and heavy quarks in hot matter by studying related phenomena in cold nuclear matter. This will be possible thanks to the variety of ion beams available for electron-nucleus collisions, that would provide an insight on how quarks and gluons lose energy and hadronize in nuclear matter.

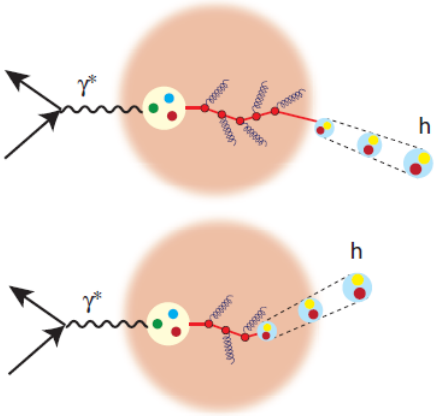

Figure 1.2: Schematic of the interaction of a parton moving through cold nuclear matter. The hadron is formed outside (top) or inside (bottom) the nucleus.

1.2 The EIC machine

1.2.1 Accelerator

The current design for the EIC uses the existing Relativistic Heavy Ion Collider (RHIC) at Brookhaven National Laboratory, the schematic of which is shown in Figure 1.3.

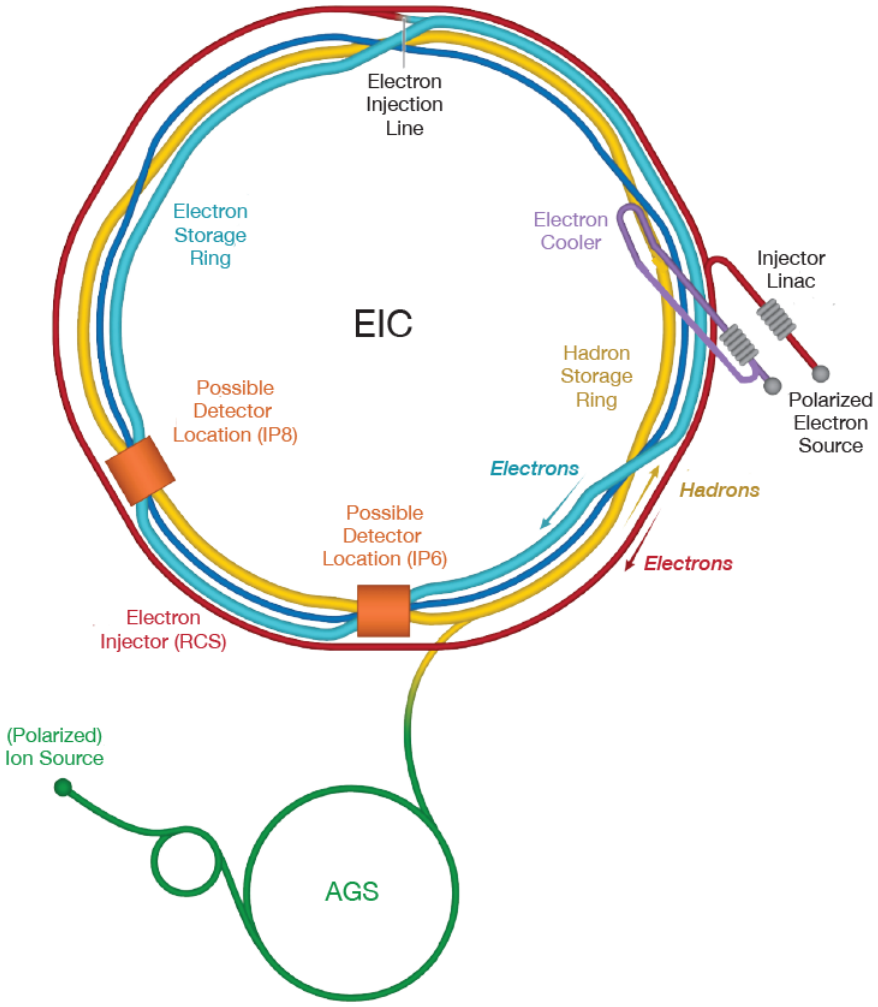

Figure 1.3: Schematic of the EIC accelerator based on the existing RHIC structure, from [2].

The features the design aims to achive are:

- High polarized electron and nucleon beams
- Ion beams from a variety of particles that range from deuteron to heavy nuclei;

- A variable enter of mass energy that ranges from ∼20 to ∼100 GeV, upgradable to ∼140 GeV;
- High collision luminosity from $\sim 10^{33}$ to $\sim 10^{34}$ $cm^{-2}s^{-1}$;
- Possibility of having multiple interaction regions.

1.2.2 Detectors

The detectors will be located at the interaction regions of the accelerator, where electron and ion beams collide. These regions must have a strong integration of forward and backward detectors, precision energy measurements, particle tracking and particle identification so that the four-vector of the final particles is known over a large range of momenta: from ∼10 MeV to ∼10 GeV. At the end of 2021 were proposed three possible detector designs: ATHENA [3], CORE [4] and ECCE [5].

The detectors are embedded into a solenoidal superconducting magnet and must be designed to operate with high efficiency even in vicinity of a large rate of background due to the circulating beams in the accelerator. Due to the asymmetry of the collision $e+p$, the hadron endcap and the electron endcap detector system see different particle types and thus the detector must have unique requirements, combined with the performance required by the region where the detector is located. The aim is to combine complementary detector technologies used in different detector concepts to achieve the full set of requirements for the region they are located in.

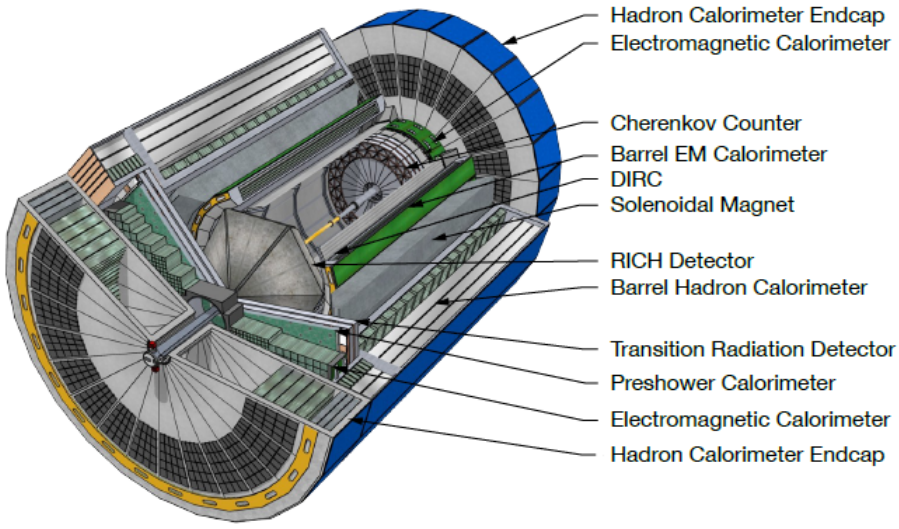

Figure 1.4: CAD model of an EIC detector concept, with tracking, particle identification and calorimetry subsystems, from [2].

Tracking and vertexing

The inner system is dedicated to tracking and vertexing. The detector design under consideration combines silicon semiconductor detector technologies to collect electron/hole pairs caused by the passage of charged particles, with gaseous tracking detector technologies to collect the ionization caused by tracks.

Particle identification: the Dual-Radiator RICH

Particle identification separates electrons from pions, kaons and protons. It is the second major system and it uses detectors based on Cherenkov light emission and time of flight to determine the originating track identity. Due to the different momentum ranges of particle in the electron endcap, barrel and hadron endcap regions, multiple radiator media are required. Details can be found in [2]. This study will focus on the dual-radiator Ring-Imaging Cherenkov detector (dRICH), shown in Figure 1.5, designed with both a gas and aerogel radiator to provide a continuous particle-identification performance from momenta of a few GeV/c up to ∼50 GeV/c.

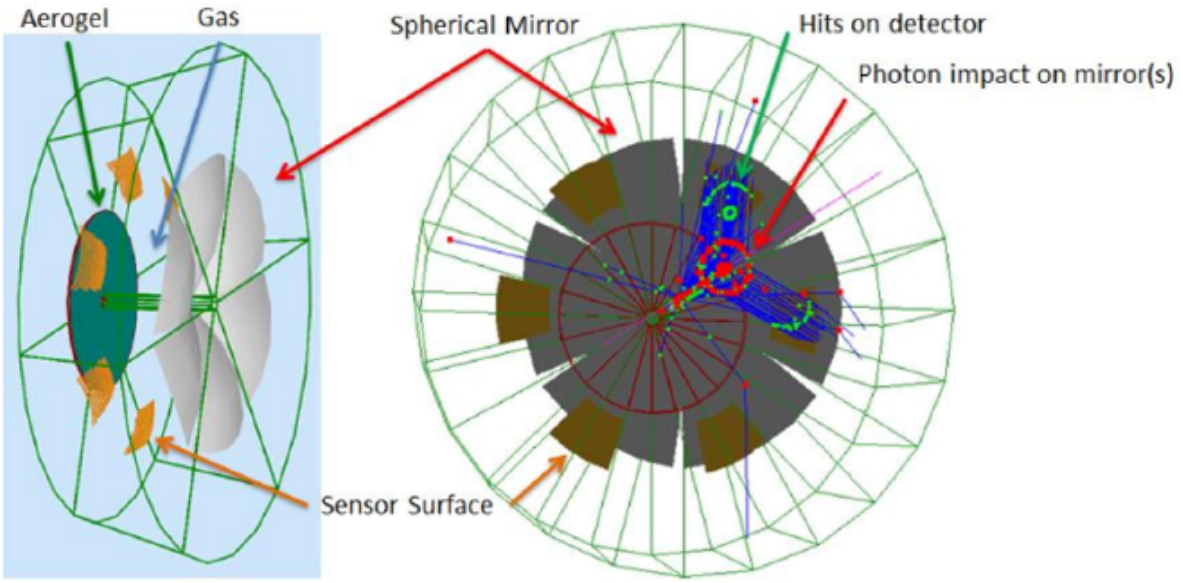

Figure 1.5: Dual RICH detector configuration, from [2]

Cherenkov radiation is emitted by particles that move in a medium at a speed greater than that of the light in that medium. The angle θ at which the light is emitted is a function of the particles speed, and it is given by

$$cos(\theta) = \frac{1}{n\beta}, \tag{1.1}$$

where n is the refractive index of the radiator medium and $\beta = \frac{v}{c}$, with c the speed of light in vacuum. A measure of the Cherenkov angle θ results in a measure of v, that combined with the momentum can determine the mass and identify the particle. Cherenkov radiation is emitted only when the speed of the particle exceeds the speed of light in the medium, $v > \frac{c}{n}$.

The dRICH consists of six identical open sectors with two radiators each, with a different refractive index (aerogel with refractive index n=1.02 and C_2H_6 gas with n=1.008), that share the same outward focusing mirror. In this area are placed highly segmented photosensors. Currently, SiPM are favored for the readout in this region of the detector.

Calorimeter

The third major detector system is calorimetry, used to measure particle energy for both electron and hadron. Due to the limited space, currently are favored short radiation lenght materials and SiPM, since they take less space and operate in the magnetic field.

Chapter 2

Single photon readout with silicon detector

This chapter is dedicated to the analysis of three pivotal components used in the experimental set-up of this study. The focus will be directed on the physical principles that allow the electronics to work, along with the technical solutions currently taken under consideration for the application in the EIC project.

2.1 Photon Detection with silicon photomultiplier

2.1.1 The PN junction and silicon photodiodes

In a pure silicon crystal, negative and positive charge carriers, respectively electrons and holes, are found in a state of steady equilibrium known as *intrinsic*. To form a photodiode, it is necessary to create a PN junction by doping a portion of the crystal with group V elements, like phosphorus or arsenic, that will act as electron donors forming an N region, and by doping the other region with group III elements, like boron or aluminium, hole donors, to form a P region. Since an electron donor atom from group V can share four electrons with neighbouring silicon atoms, they can form an electrocovalent bond and participate in the silicon crystal by donating its fifth outermost electron to the conduction band. An acceptor atom shares three of its electrons with the silicon atoms and becomes part of the crystal by introducing a hole. All of the atoms in the crystal share the same conduction and valence band, so the electrons and holes can move freely by Brownian random walk when there is no external electric field.

In the PN junction thus formed, there is a concentration gradient between the majority carriers of the two regions, creating a diffusion current of electrons moving in the direction of the P side and holes to the N side in order to recombine and forming in the area surrounding the junction a *depletion layer*. A schematic of the PN junction is

depicted in Figure 2.1. As a consequence of the recombination, the depletion layer in the N region becomes positively charged due to the electrons loss, and the depletion layer in the P region becomes negative. These charges create an internal electric field pointing from the N side towards the P side, with an absolute intensity peak at the PN junction. The charge carrier flow quickly stops, reaching the equilibrium when the force exerted by the electric field, opposite to the carrier direction of movement, equals in magnitude the diffusion process.

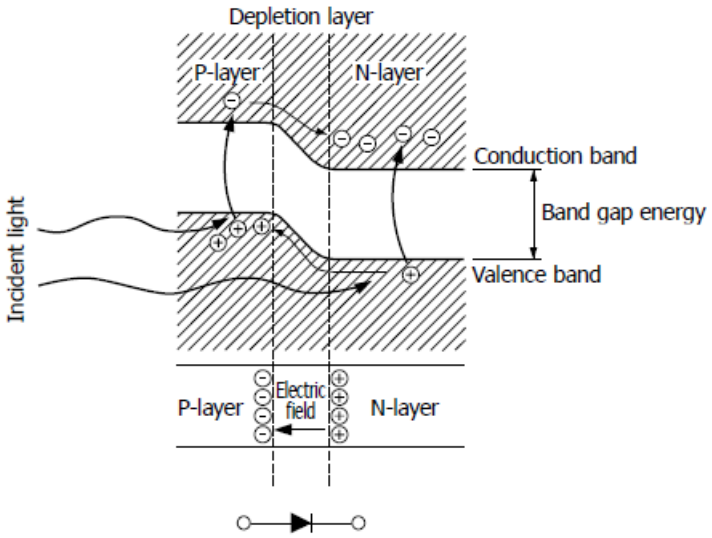

Figure 2.1: Schematic of a PN junction, from [6].

The equilibrium can be broken by either thermal agitation or photoelectric effect. This kind of disturbance creates an excess of charge carriers in either side of the depletion layer, thus forming a current across the junction. An electron in the valence band gains enough energy to move to the conduction band, leaving a hole behind. This electron-hole pair is not compensated by any charge in the atoms forming the crystal and are considered excess charge carriers. Due to the presence of the electric field, each charge carrier moves in the direction of its majority charge, electrons towards the N region and holes towards the P region. As a consequence, only the minority charge carriers move across the junction and reach the depletion region edges, while the majority carriers do not cross the junction and remain in their native region. This process creates a minority carrier current.

The depth of the depletion layer is responsible for the wavelength of the light absorbed by the crystal, and thus it affects the photosensitivity and frequency response of the photodiode. By increasing the depth of the depletion region, the sensitivity towards longer wavelengths increases, and so does the ability of collecting thermally-generated carriers, that forms the dark current.

If the electric field within the depletion layer is sufficiently high, a charge carrier can be accelerated until it reaches enough kinetic energy to create a secondary electron-hole pair. This process is called *impact ionization* and a single absorbed photon can trigger a cascade that will spread through the silicon crystal, amplifying the initial pair into a macroscopic current.

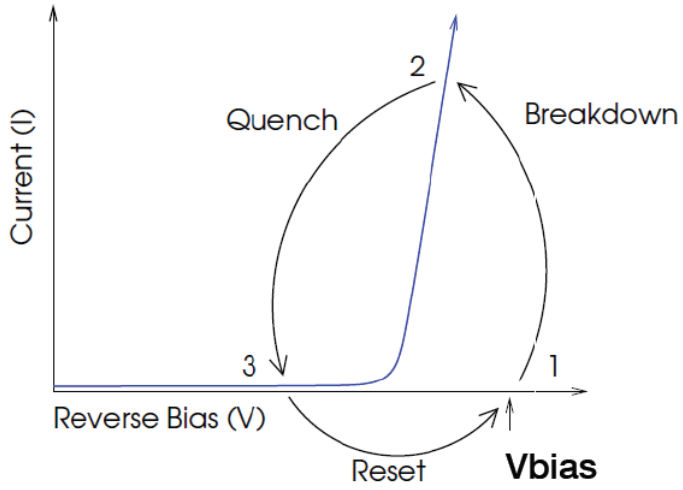

Figure 2.2: Current as a function of the supplied voltage. The breakdown, quench and reset cycle of a SPAD is shown in black, from [7].

This process is called Geiger discharge, and a photodiode operating in this regime is referred to as a Single Photon Avalanche Diode (SPAD). The desired electric field is achievable by applying a reverse bias voltage greater than the nominal breakdown voltage. Through a series resistor the current can be quenched, lowering the voltage below the breakdown value thus stopping the avalanche in order to let the diode detect the next photons (Figure 2.2). The diode described can be seen as a photon-triggered switch.

2.1.2 Silicon photomultiplier

A silicon photomultiplier (SiPM) consists of an array of independent SPAD sensors, each connected to its own quenching resistor, as shown in Figure 2.3. When a microcell, consisting of a photodiode and its resistor, absorbs a photon, an avalanche is initiated, creating a current through the microcell. This triggers the action of the resistor, that quenches the photocurrent limiting the avalanche. The voltage across the diode returns to the nominal value in a time called *recovery time*. The avalanche caused by the photon

absorption is limited to the single microcell that sees the event, while the other microcells will remain ready to detect photons.

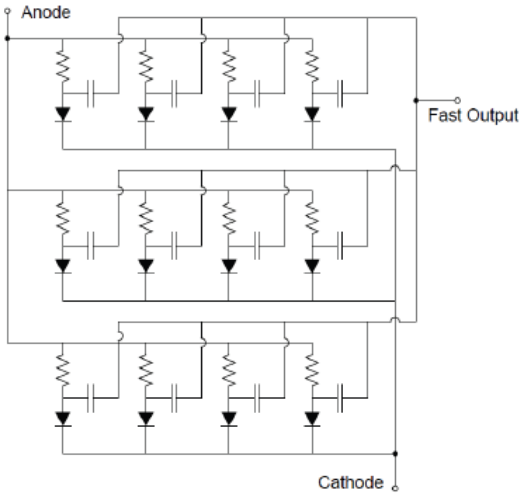

Figure 2.3: A simplified circuit of an SiPM, consisting of an array of photodiodes and quenching resistor, from [7].

A typical SiPM output pulse, shown in Figure 2.4, presents a rise time that is determined by the formation of the avalanche, by the variation in the transit times of the signals generated in different points of the sensor and by the output impedance of the sensor. The recovery time of the cell depends on the microcell recharge time constant, given by

$$\tau_{RC} = C_d(R_q + R_s \cdot N), \tag{2.1}$$

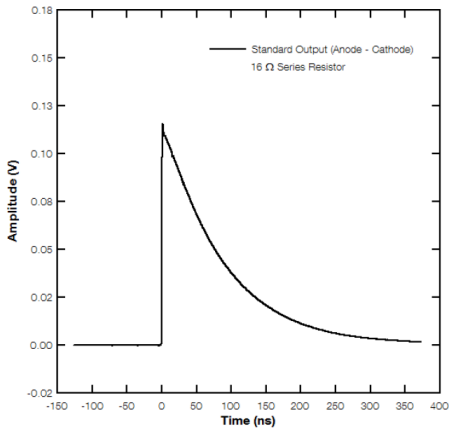

Figure 2.4: Output pulse showing the recovery time of the cell, from [7].

where C_d is the effective capacitance of the microcell, R_q is the value of the quench resistance, R_s is any resistance in series with the sensor and N is the number of microcells. The capacitance varies with the size of the cells, the larger the cell, the greater the recovery time.

The percentage of area of the sensor sensitive to light is called *fill factor*. Since for both electrical and optical isolation, the cells must be separated from each other when forming the sensor, and some of the area is dedicated to the resistor, the surface of the sensor presents some dead space. The space required by the resistor is constant, this means that larger cells result in a higher fill factor. The importance of the fill factor will be discussed in section 2.1.3 while examining the efficiency and gain parameters of the SiPM.

2.1.3 Performance parameters

The following performance parameters are essential to operate a silicon photomultiplier in order to obtain the desired data.

Breakdown voltage and gain

As mentioned in the section above, the breakdown voltage is the bias value at which the Geiger avalanche starts. To identify the breakdown voltage on a square root of the dark current versus bias graph, it is sufficient to plot a straight line fit and find the intercept, as shown in Figure 2.5.

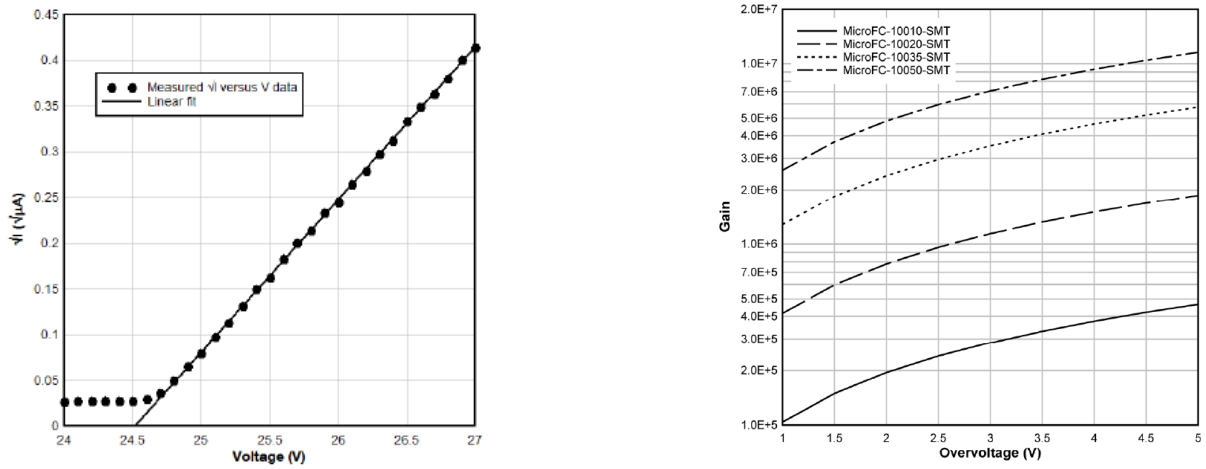

Figure 2.5: (Left) Square root of the dark current versus bias voltage, the intercept is the breakdown voltage. (Right) Gain as a function of overvoltage for different sizes of microcells.

SiPMs are operated at a bias higher than the breakdown voltage, and the difference between the bias point and the breakdown is referred to as *overvoltage*.

The charge created by the cell for each detected photon, the gain, is a function of the overvoltage and the microcell size. The amount of charge generated by each microcell at every avalanche is uniform, the gain can be calculated knowing the overvoltage and the cell capacitance and it is defined by the ratio of the charge from an activated cell and the electron charge:

$$G = \frac{C \cdot \Delta V}{q}. \tag{2.2}$$

In Figure 2.5 the gain of the microcell at different sizes is shown.

Photon detection efficiency

The photon detection efficiency (PDE) measures the sensitivity of the photomultiplier and it depends on the wavelength of the incident light, the overvoltage and the fill factor F as follows:

$$PDE(\lambda, V) = \eta(\lambda) \cdot \epsilon(V) \cdot F. \tag{2.3}$$

It represents the statistical probability that an incident photon will produce an avalanche in the target microcell. The variable $\eta(\lambda)$ is the quantum efficiency, a measure of the probability for an incident photon to create and electron-hole pair in the sensor, while the variable $\varepsilon(\mathrm{V})$ is the avalanche initiation probability and takes into consideration that not all charge carriers will initiate the avalanche.

The PDE is often calculated as a function of the responsivity of the sensor R, given by the average photocurrent produced per unit of optical power at a particular wavelength. The resulting expression of the PDE is

$$PDE = \frac{R \cdot h \cdot c}{\lambda \cdot G \cdot e \cdot (1 + P_{AP}) \cdot (1 + P_{XT})} \cdot 100\%, \tag{2.4}$$

where $\mathrm{P_{AT}}$ and $\mathrm{P_{XT}}$ are respectively the afterpulse and the crosstalk probability, that will be discussed more in depth in the next paragraph. h is the Planck constant, c is the speed of light, λ is the wavelength and e is the elementary charge.

Optical crosstalk and afterpulse

The optical crosstalk between microcells is a function of overvoltage and the fill factor of the cell, and it is a component of the SiPM noise. This phenomenon is generated when the charge carriers in the avalanche initiate a secondary avalanche in a near microcell. Usually the wavelength of these secondary photons is in the near infrared region. As a consequence of the crosstalk, a single incident photon can generate a signal equivalent to

two or three photons. The crosstalk increases with overvoltage due to the higher amount of carriers that cross the junction.

The term afterpulse refers to the delay of the avalanche when a carrier becomes trapped in a defect of the crystal. If the delay is short compared to the recovery time, the afterpulse can be neglected, but it can impact measurements if the rate is high. To minimize the afterpulse the constructor must minimize the defect in the silicon sensors.

Dark count rate

The dark count rate (DCR) is generated by the thermal electrons, as mentioned at the beginning of this section. The DCR is the primary source of noise in an SiPM and it is a function of the overvoltage and the temperature. When a thermally-generated electron initiates an avalanche, that results in a signal identical to the one produced by the incident photons. By setting a threshold above the single photon level, this noise can be reduced, but it will still contribute to the measured signal. The DCR can be measured by setting a threshold at half-photon level. The count increases with the voltage and with the temperature.

Temperature dependency

As stated above, the DCR, along with the breakdown voltage, is affected by the temperature. The dependence of the breakdown voltage from the temperature is linear and must be taken under consideration when the temperature fluctuations are large and not compensated for they can affect the overvoltage. Bias compensation is the most simple way to stabilize the thermal conditions.

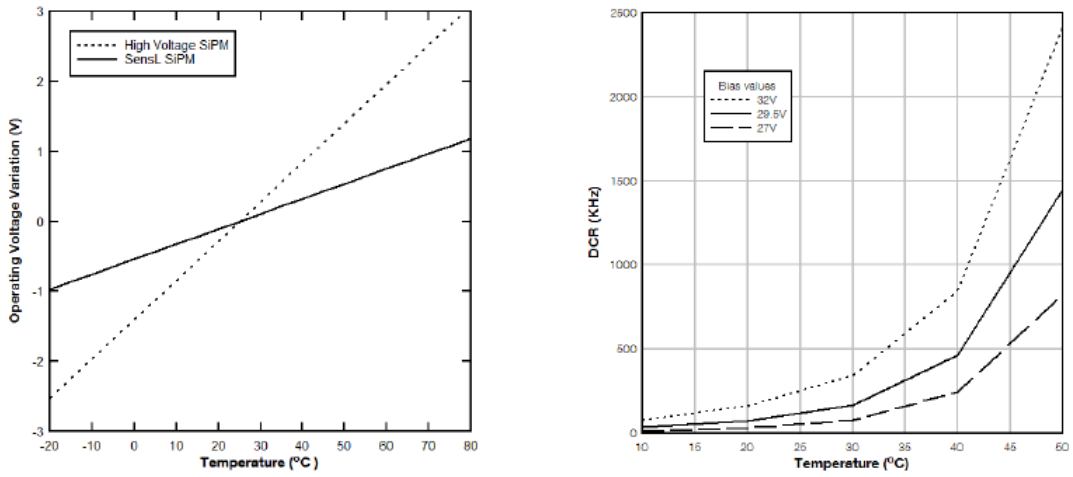

Figure 2.6: (Left) Overvoltage as a function of the temperature. The dependency is linear. (Right) DCR as a function of the temperature.

While most parameters will remain constant when the overvoltage is constant, the DCR is affected by the temperature fluctuations regardless, since they can change the number of thermal-generated electrons. Actively cooling the photomultiplier can reduce significantly the DCR. In Figure 2.6 are shown the dependence of the overvoltage (left) and the dark count rate (right) from the temperature.

2.1.4 Radiation damage

The effect of radiations to silicon detectors can cause two types of damage: bulk damage due to non ionizing energy loss (NIEL), and surface damage due to ionizing energy loss (IEL). Damages in the detector cause an increase in the dark current, and thus in the dark count rate.

Bulk damage is produced by high energy particles, such as protons, neutrons, electrons and photons, that can displace atoms in the crystal creating defects. The minimum energy transfer necessary to cause this type of damage is $\sim$25 eV. For energies >1 keV the displaced atom can move other atoms forming a cluster defect. Interstitials and vacancies, left behind by displaced atoms, are very mobile for temperatures above 150 K and can annihilate with each other curing the defects. This process can be sped up by increasing the temperature of the sensor, a procedure called annealing. Surface damage is caused by photons and charge particles with energies below 300 keV. In the oxide SiO_2, X-rays produce one electron-hole pair every 18 eV. A fraction of these pairs recombine, while the remaining pairs move by diffusion in the oxide. Most electrons can leave the crystal, while holes remain creating interface traps that, if exposed to an electric field, can generate a surface current and therefore increase the dark count rate below the breakdown voltage. More on this subject in [8].

2.2 Peltier modules

Peltier modules are a thermal management solution used to cool an object or to keep it at a specific temperature. The technology behind these modules is based on the Peltier effect, one of the three known thermoelectric effects, that will be discussed in the following sections as well as an overview on the main components of a Peltier module.

2.2.1 Peltier effect

When a potential difference, and thus a current, is applied to the two materials forming a thermocouple, the two junctions gain a different temperature. This is called Peltier effect, opposite of the Seebeck effect, and it can be used to cool a region by placing the hot junction outside an insulated area, and the cold junction inside the area meant to be cooled. This cooling method allows to refrigerate an area with no circulating fluids or

moving parts. Peltier modules do not absorb thermal energy, they only transfer it from the cold side of the module to the hot one, where it dissipates [9].

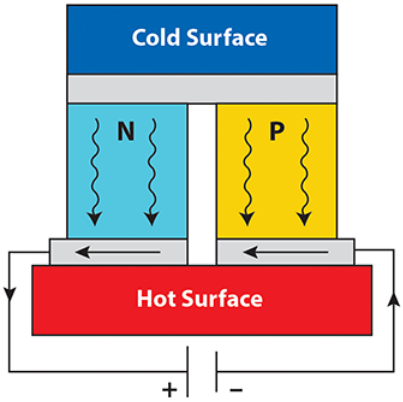

Figure 2.7: Schematic of a thermoelectric cooler based on Peltier effect [10].

2.2.2 Structure of a thermoelectric cooler

A Peltier module, as the schematic shows in Figure 2.8, consist of Bismuth Telluride semiconductor pellets, connected electrically in series but thermally in parallel, which are doped so that either the positive or negative charge carrier is responsible for the majority of the current. The platform that acts as a base for the pellets and the conductive tabs is made of metalized ceramic and the semiconductor elements are solded to the electrical interconnect made of copper.

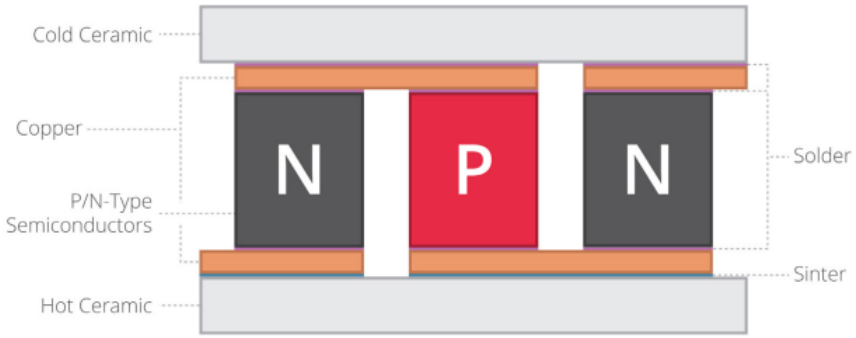

Figure 2.8: Peltier module structure.

A heat sink is placed at the opposite side of the heat source, in order to absorb the heat on the hot side of the Peltier module and dissipate it to the surrounding air. The heat sink is designed to dissipate not only the heat from the source, but also the heat

produced inside the Peltier element during heat pumping. To achieve the minimal total heat dissipated by the heat sink, the Coefficient of Performance (COP), defined as

$$COP = \frac{Q_C}{P_{el}}, \tag{2.5}$$

where Q_C is the heat absorbed at the cold side and P_{el} is the input power of the Peltier element, must be maximized, thus minimizing the power supplied to the module.

To regulate the temperature of an object, the Peltier element must be combined with a Thermoelectric Cooling (TEC) controller that provides the current. By changing the direction of the current, one can switch from cooling to heating the area of interest. To regulate the temperature of the object, the TEC control compares the actual and some recent temperature with the target value, in order to provide the right amount of current to the thermoelectric element.

When operating a Peltier module, the maximum temperature available is 200°C, due to the melting point of the solders (currently are considered SbSn solders, with a melting point of 235°C). There is also a current limit after which the temperature will rise again due to the dissipation of power, as shown in Figure 2.9 [11].

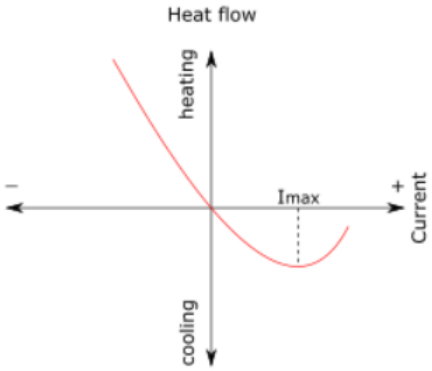

Figure 2.9: Characterization of the heat flow in a Peltier element as a function of the current supplied by the TEC control.

2.3 ALCOR

The prototype used to readout SiPM at cryogenic temperatures currently under consideration is ALCOR (A Low-power Circuit for Optical Readout), a 32-pixel mixed-signal application specific integrated circuit (ASIC) based on CMOS technology [12].

Pixels are placed in a matrix structure of 4 rows and 8 columns, shown in the CAD layout in Figure 2.10, and each pixel is designed with a regulated common gate used for communication between the sensor and the rest of the chain.

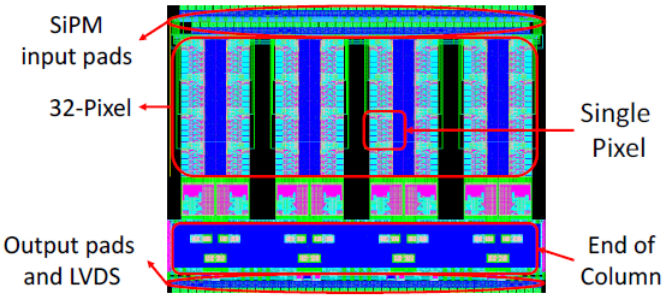

Figure 2.10: CAD layout architecture of ALCOR.

The signal, through two amplifiers, reaches two leading edge discriminators that generate the trigger CMOS signals, that is fed to the pixel digital control block. For each signal is generated a time stamp from a binary 15-bit coarse counter and from a 9-bit time-to-digital converter (TDC), that measures the difference between the time stamp and the next clock rising edge. A pixel generates a 32-bit word when a photon is detected.
The word contains:

- 3 bits for column position tag
- 3 bits for pixel position tag
- 2 bits for TDC address
- 15 bits for coarse counter
- 9 bits for fine counter

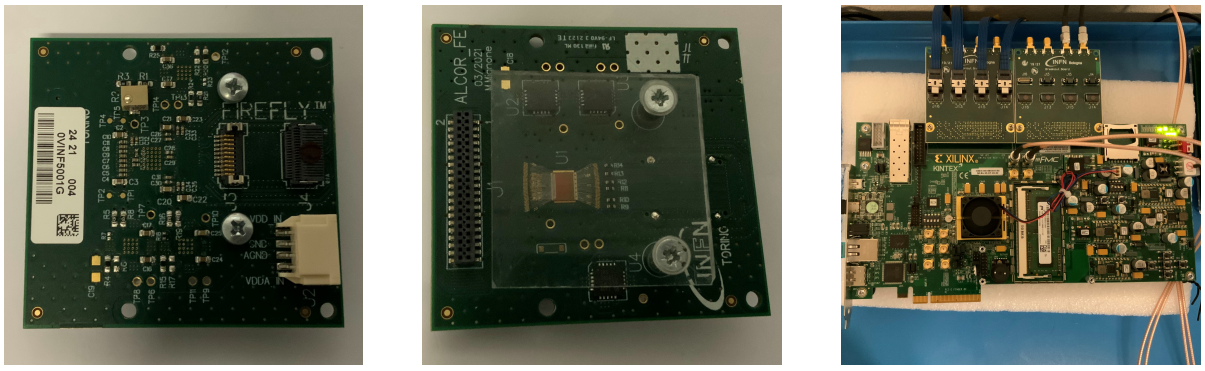

(a) Front (b) Back (c)

Figure 2.11: Both sides of one of the ALCOR board (a, b) and the FPGA (c) used in the set-up.

Data from each pixel are collected by the End-of-Column and via LVDS (Low-Voltage Differential Signaling) drivers they can be transmitted off-chip. The front-end and pixel operation mode can be configured by a FPGA. In Figure 2.11 is shown one of the ALCOR used in the experimental set-up of this study, along with the FPGA.

Chapter 3

Setup and results

The aim of this study is to compare the dark count rate of four different types of SiPM sensors measured in a climatic chamber and in the prototype dRICH readout box with thermoelectric cooling. The two experimental setups will be discussed in Section 3.1, while Section 3.2 will focus on the characterization of the measurements and how the different cooling techniques, the thermoelectric cooling and the climatic chamber, affect the DCR. In Section 3.3 will be analyzed the effect of a flexible PCB on the dark count rate, comparing the measurements with and without the PCB taken inside the climatic chamber.

3.1 Experimental setup

As mentioned in Section 2.1.3, the dark count rate of an SiPM decreases with the temperature. To obtain the optimal conditions for the measurements, the sensors have been kept at a temperature of -30°C both inside the climatic chamber and in the readout prototype using the Peltier elements.

Prototype EIC readout with thermoelectric cooling

The prototype setup consist of a box containing the equipment necessary for the cooling and data acquisition of the four SiPM boards, as shown in Figure 3.1:

- the four boards on which the SiPMs are mounted;
- four adapter boards to regulate the voltage supplied to the SiPMs;
- four ALCOR boards for the data acquisition;
- two Peltier elements, placed so that the cold side is directly under two of the boards in order to cool them, and the hot side is in contact with the water cooling system (see Figure 3.2);

- a digital-output relative humidity and temperature sensor DHT-22.

The boards under test mount two different types of sensors on the even and odd channels, as listed in Table 3.1. The difference between the sensors will become relevant in the next section while analyzing the data. On each of the SiPMs boards is also mounted a temperature sensor LM73.

	HAMAMATSU 1	HAMAMATSU 2	FBK	SENSL
Even	S13360-3050VS	S14160-3050HS	NUVHD-CHK	MicroFJ30020TSV
Odd	S13360-3025VS	S14160-3015PS	NUVHD-RH	MicroFJ30035TSV

Table 3.1: Sensor models for even and odd channels on the four boards under test.

Outside of the box, the set-up consist of:

- four Master Logic for communication with the adapter boards;
- an FPGA to program and read the ALCOR data;
- a QL355TP power supply for the front-end boards;
- a TSX1820P power supply used to bring power to the Peltier elements;
- a PLH250-P power supply used to bring the high voltage to the sensors;
- a dew point analyzer Systech 410;
- a water cooling system to cool the hot side of the Peltier element, a refrigerated circulator HAAKE C41P;
- a heatless regenerative desiccant dryer KAESER DC 2.0.

The web application Grafana has been used to monitor the conditions inside the box and to operate the elements inside. Through specially programmed buttons, one could start and stop the measurement, turn on and off the power supplier, change the temperature and have an overview of the current state of every component of the set-up.

Climatic chamber

The set-up was placed inside the climatic chamber MEMMERT CTC256 that controlled the temperature, while the desiccant kept the air humidity low. That was necessary to avoid going above the dew point while testing at -30°C. The set-up inside the climatic chamber is identical to the one inside the prototype box, the only difference is the cooling system.

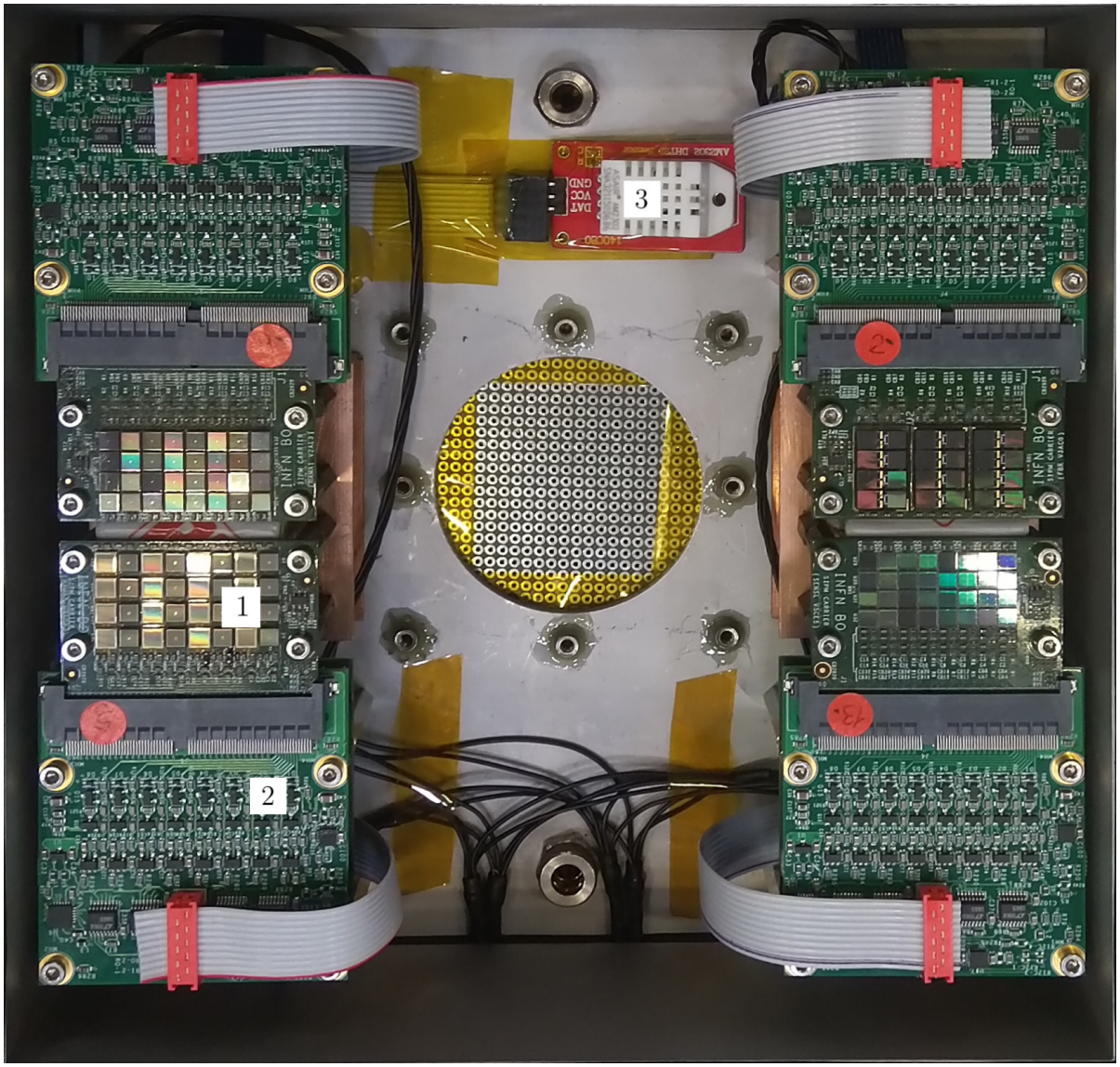

Figure 3.1: Set-up of the prototype EIC readout with thermoelectric cooling. The picture shows the boards on which are mounted the SiPMs (1): HAMAMATSU S13360 (top left), HAMAMATSU S14160 (bottom left), FBK (top right) and SENSL (bottom right). Also in the picture the adapter boards (2) and the humidity and temperature sensor (3).

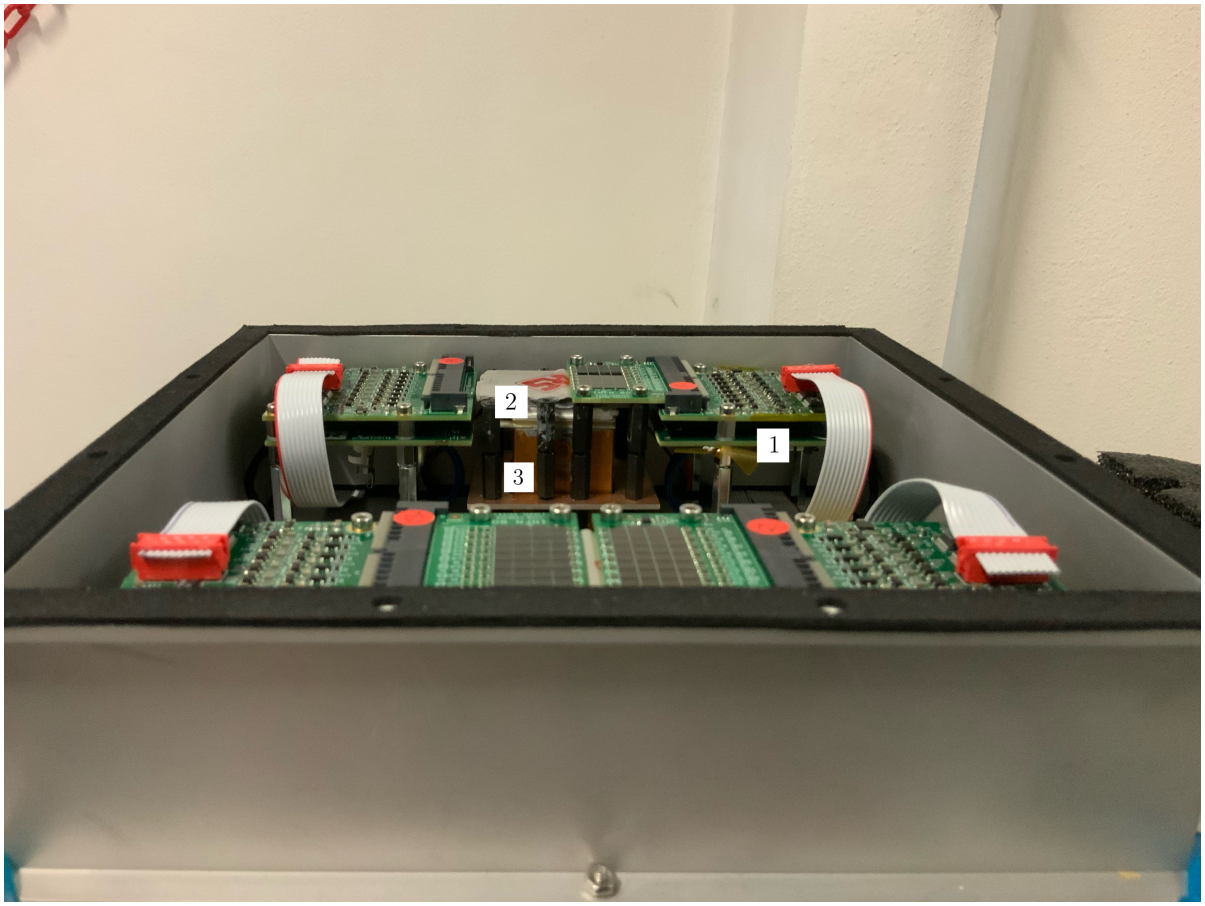

Figure 3.2: View of the prototype set-up from the side: the ALCOR boards under the adapters (1), the Peltier element (2) and the water cooling system (3).

3.2 Characterization

3.2.1 Performance comparison at -30°C

For each of the four different SiPM boards, the measurements of the dark count rate have been taken inside the climatic chamber and inside the prototype with thermoelectric cooling, both set at -30°C. For each value of the bias voltage were taken 25 measurements of the dark count rate, each point in the bias voltage scan plots is the mean value and the error is the one associated to the mean value. Even and odd rows have been analyzed separately since they mount different sensors. Shown in the figures below, the dark count rate of one of the sensors as a function of the bias voltage and the mean relative rate difference, found as the mean value of

$$\frac{DCR_{prototype} - DCR_{climatic\,chamber}}{DCR_{climatic\,chamber}}, \tag{3.1}$$

as a function of the bias voltage fit with a constant function in the operative range of bias voltage. The points on the plot represent the mean value of the relative rate difference averaged over all sensors at that bias voltage, the error bars are the error associated with the mean value while the bands represent the RMS dispersion of the sample. For each of the eight types of sensors, two on each board, the $\tilde{\chi}^2 = \frac{\chi^2}{n_{DOF}}$ is small enough to assert that the mean relative rate difference is constant.

HAMAMATSU S13360

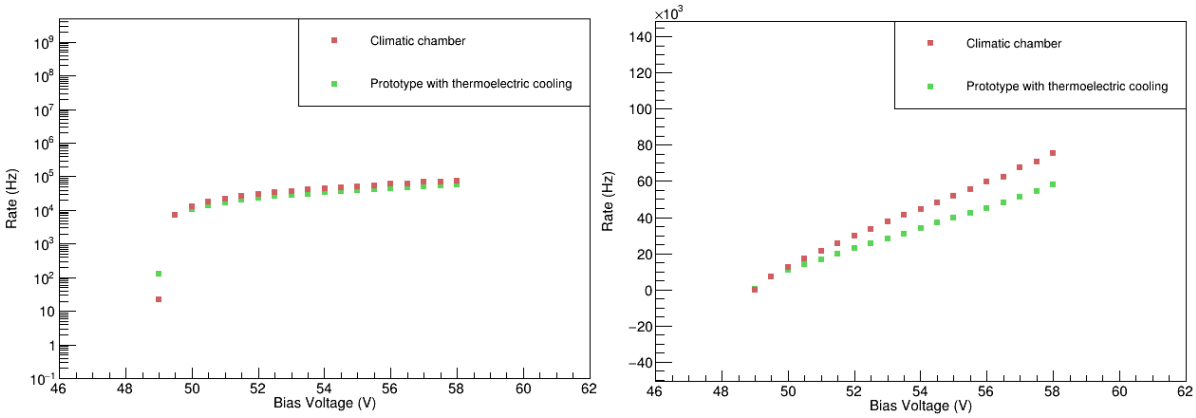

Figure 3.3: Dark count rate as a function of the bias voltage with semi-logarithmic plot (left) and linear plot (right) for one HAMAMATSU S13360-3050VS sensor (channel A1).

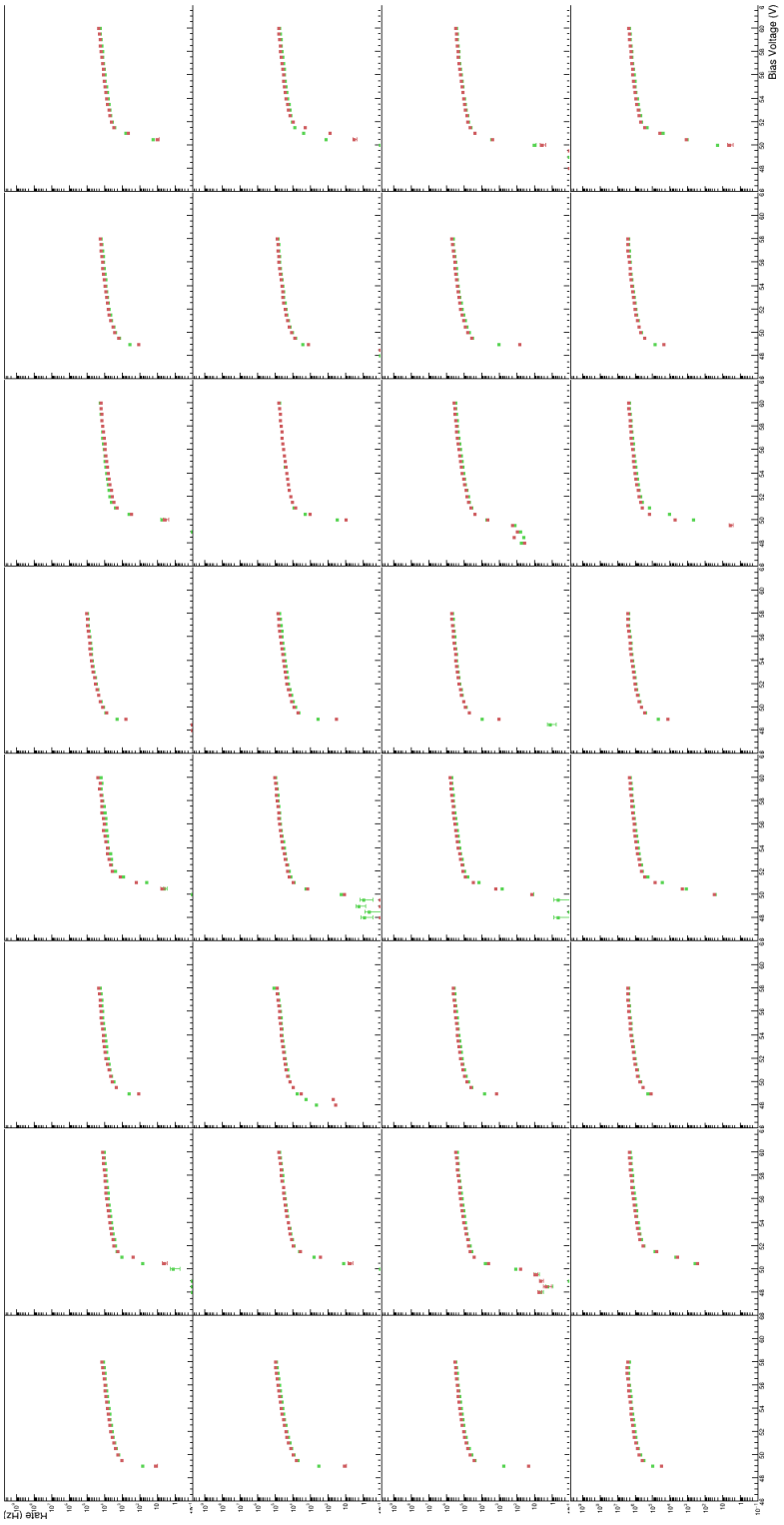

Figure 3.4: Dark count rate as a function of the bias voltage for all the 32 sensors on the HAMAMATSU S13360 board.

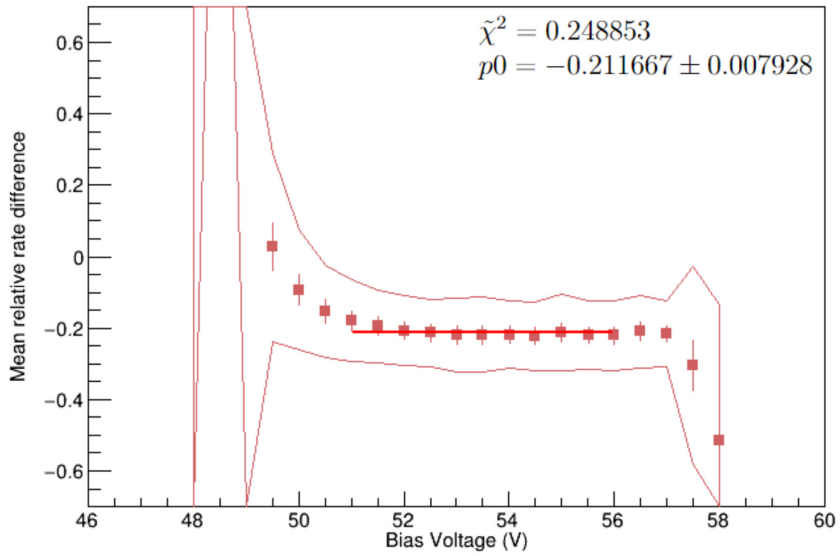

(a) Even rows of sensors S13360-3050VS.

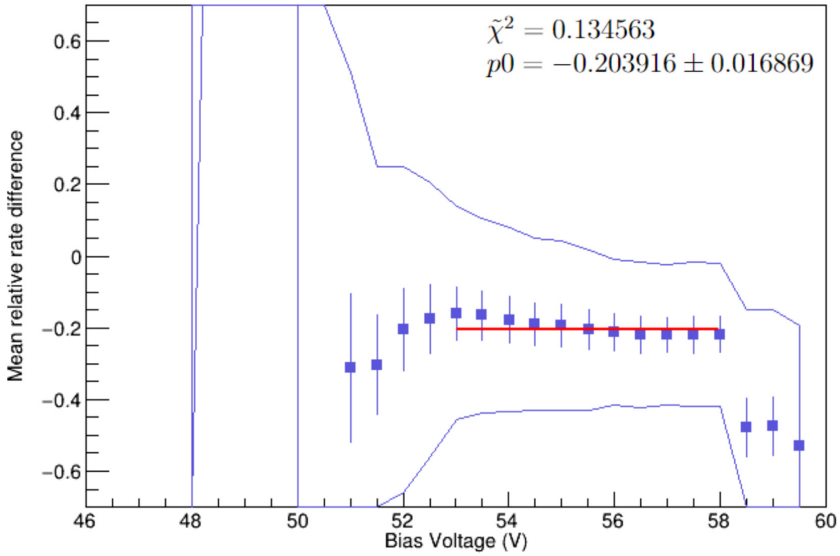

(b) Odd rows of sensors S13360-3025VS.

Figure 3.5: Mean relative rate difference as a function of the bias voltage for even (a) and odd (b) sensors. The plot also shows the fit parameters $p0$, mean relative rate difference, and the $\tilde{\chi}^2 = \frac{\chi^2}{n_{DOF}}$.

HAMAMATSU S14160

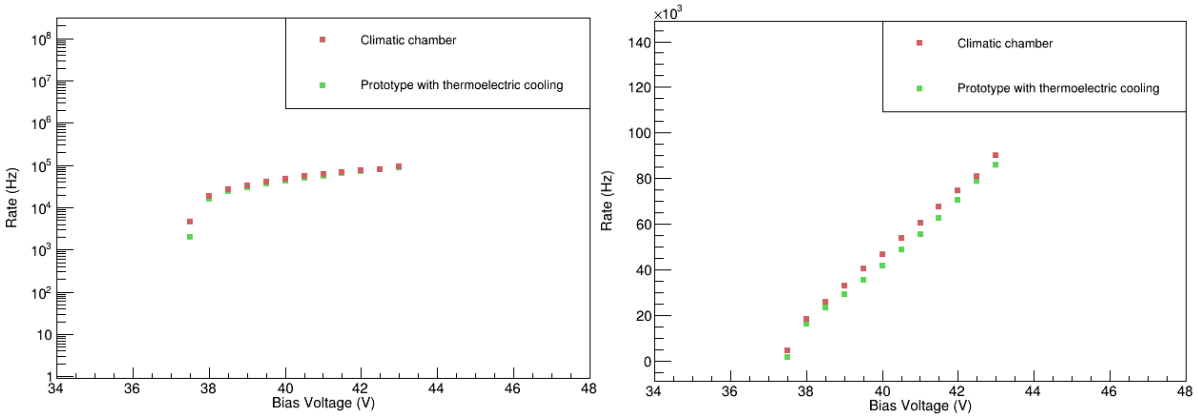

Figure 3.6: Dark count rate as a function of the bias voltage with semi-logarithmic plot (left) and linear plot (right) for one HAMAMATSU S14160-3050HS sensor (channel A1).

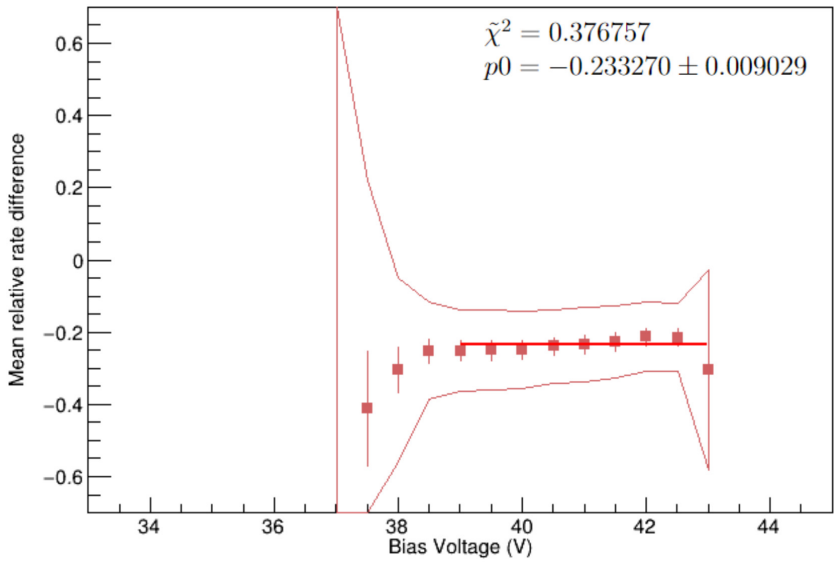

(a) Even rows of sensors S14160-3050HS.

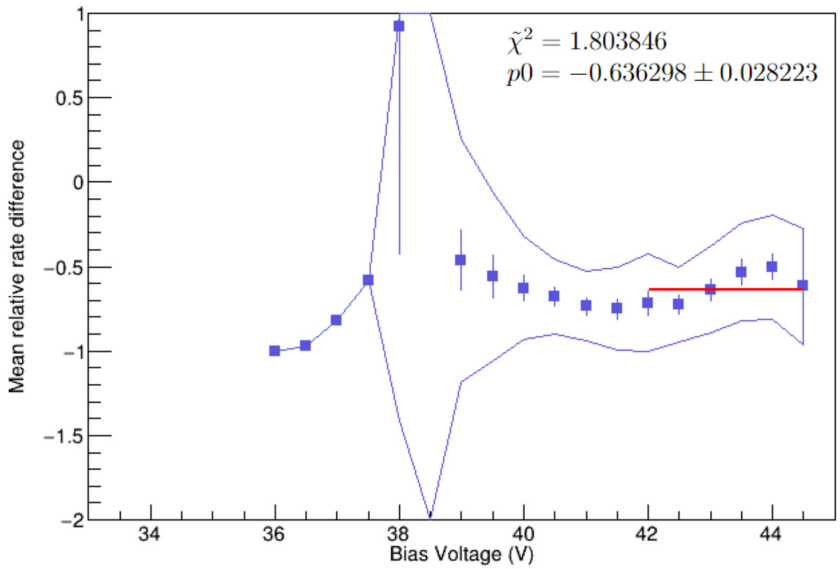

(b) Odd rows of sensors S14160-3015PS.

Figure 3.7: Mean relative rate difference as a function of the bias voltage for even (a) and odd (b) sensors. The plot also shows the fit parameters $p0$, mean relative rate difference, and the $\tilde{\chi}^2 = \frac{\chi^2}{n_{DOF}}$.

FBK

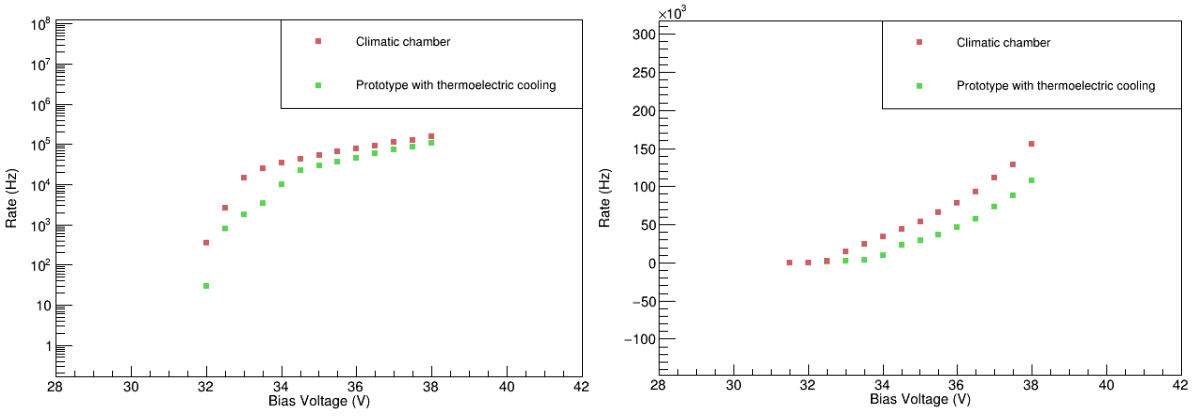

Figure 3.8: Dark count rate as a function of the bias voltage with semi-logarithmic plot (left) and linear plot (right) for one NUVHD-CHK sensor (channel A1).

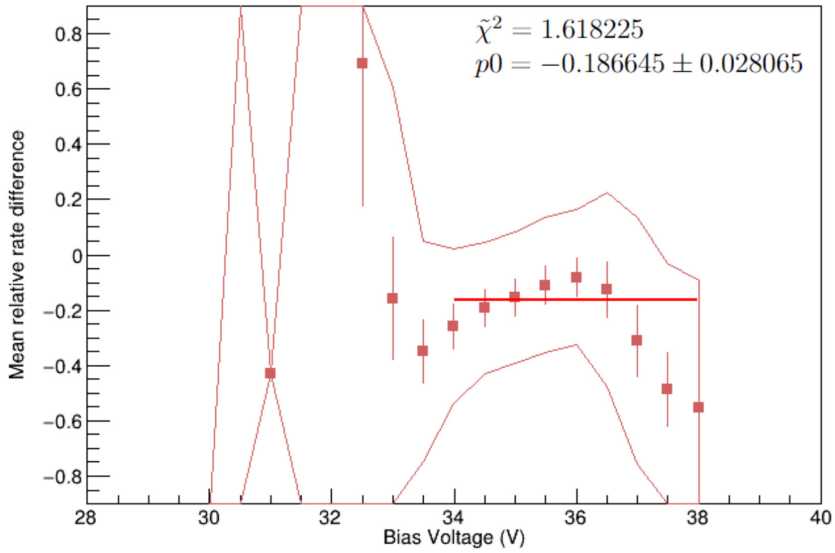

(a) Even rows of sensors NUVHD-CHK.

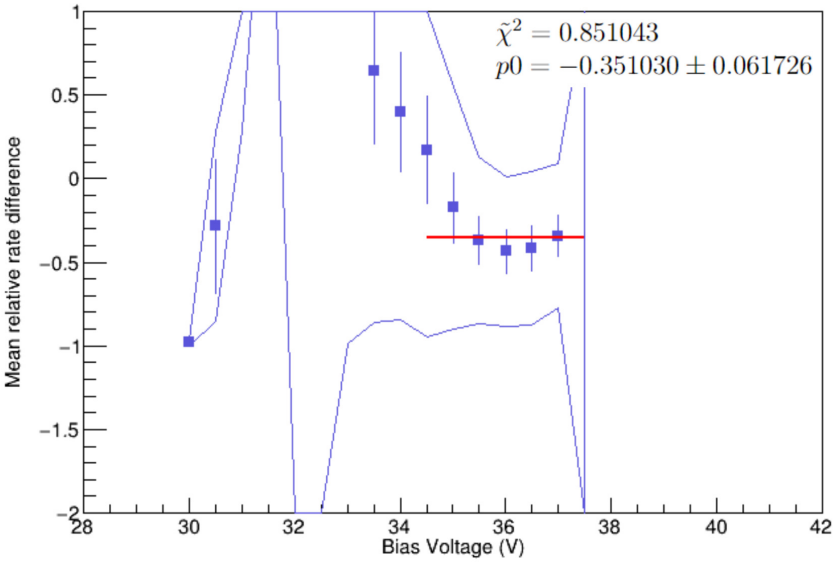

(b) Odd rows of sensors NUVHD-RH.

Figure 3.9: Mean relative rate difference as a function of the bias voltage for even (a) and odd (b) sensors. The plot also shows the fit parameters $p0$, mean relative rate difference, and the $\tilde{\chi}^2 = \frac{\chi^2}{n_{DOF}}$.

SensL

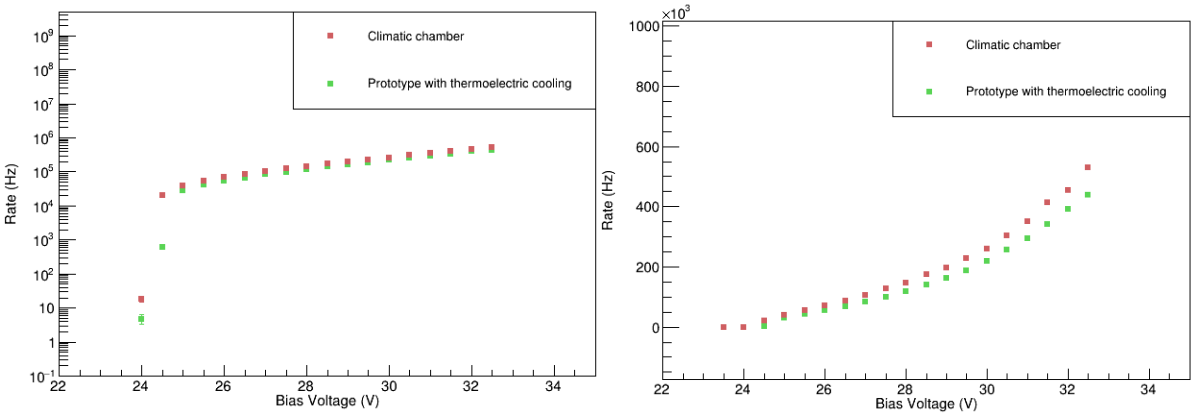

Figure 3.10: Dark count rate as a function of the bias voltage with semi-logarithmic plot (left) and linear plot (right) for one MicroFJ-30020-TSV sensor (channel A2).

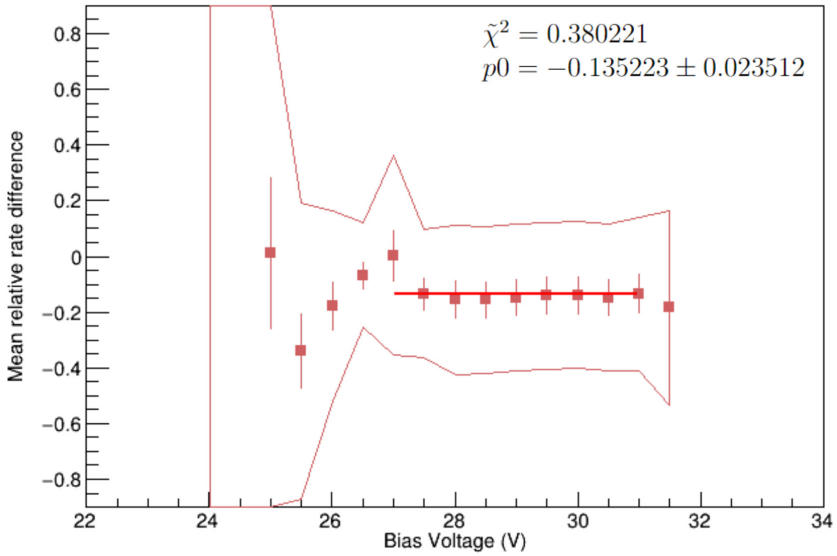

(a) Even rows of sensors MicroFJ-30020-TSV.

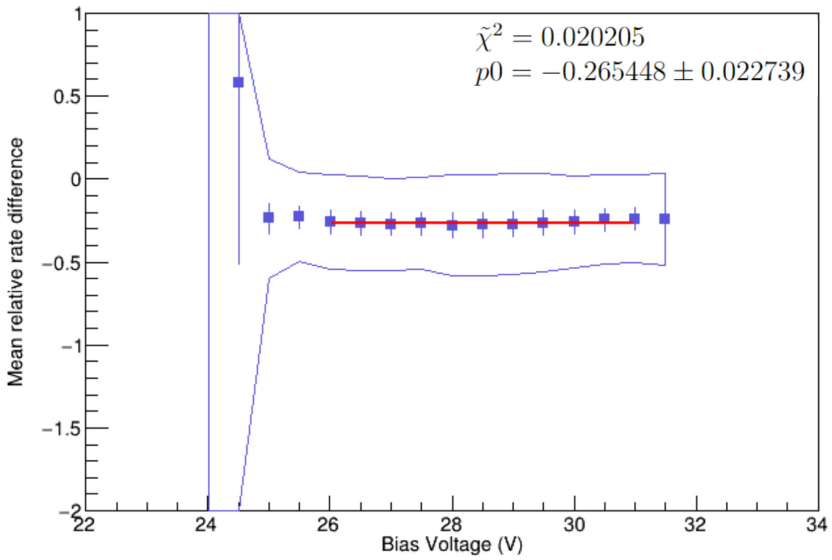

(b) Odd rows of sensors MicroFJ30035TSV.

Figure 3.11: Mean relative rate difference as a function of the bias voltage for even (a) and odd (b) sensors. The plot also shows the fit parameters $p0$, mean relative rate difference, and the $\tilde{\chi}^2 = \frac{\chi^2}{n_{DOF}}$.

3.2.2 Performance comparison at -32.9°C

The plots in Section 3.2.1 reveal a difference in the dark count rate measured in the climatic chamber and in the prototype box with thermoelectric cooling, the first being surprisingly the highest. After taking into consideration the temperature of the climatic chamber and the temperature measured by the LM73 sensors mounted on the boards while taking the measurements in the climatic chamber, a discrepancy was revealed. As shown in Figure 3.12, the temperatures are identical up until 16:30 circa, when the electronics were turned on. The temperature on the sensors then rises by approximately 2.5°C as a consequence of the vicinity of the electronics, while the temperature measured inside the climatic chamber is significantly lower. We therefore inferred that the measurements taken in the climatic chamber were taken with sensors at -27.5°C instead of -30°C, hence the origin of the small discrepancy with the readout box.

The measures of dark count rate for the HAMAMATSU S13360 were then taken again by setting the climatic chamber at a temperature of -32.9°C, resulting in a temperature of -30°C on the SiPM boards when the electronics are turned on, thus matching the temperature of the boards when the DCR measures are taken inside the prototype with thermoelectric cooling.

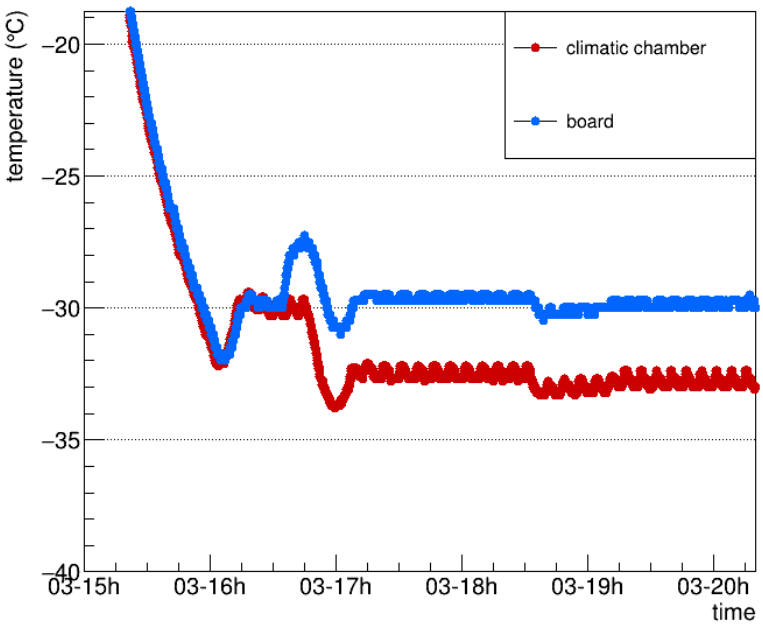

Figure 3.12: Temperature measured by the climatic chamber (red) and by the LM73 sensors on the SiPM boards (blue).

Figure 3.14 shows a mean relative rate difference between the DCR measured inside the climatic chamber set at -32.9°C and the DCR measured with the thermoelectric cooling system set at -30°C smaller than the one obtained with the measure taken with the climatic chamber set at -30°C. The difference went from 25% (Figure 3.5) to 5%.

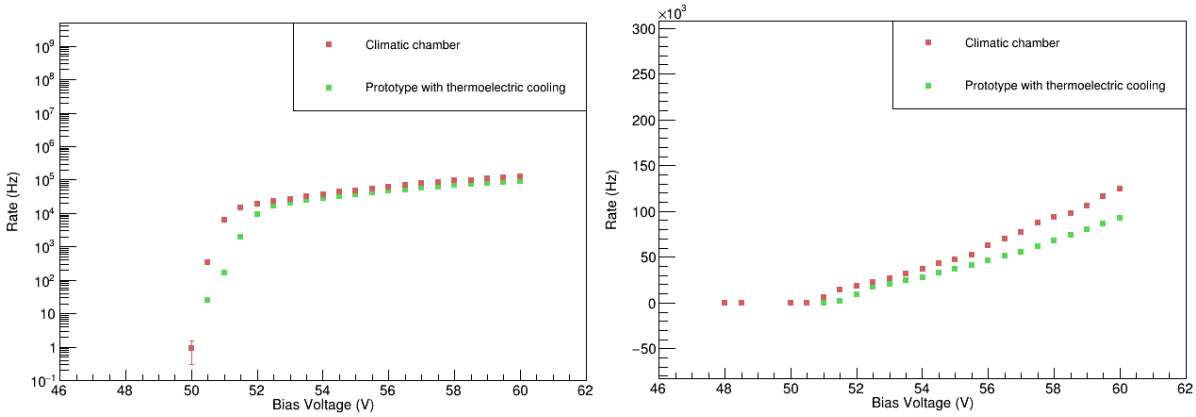

Figure 3.13: Dark count rate as a function of the bias voltage with semi-logarithmic plot (left) and linear plot (right) for one HAMAMATSU S13360-3050VS sensor (channel A1).

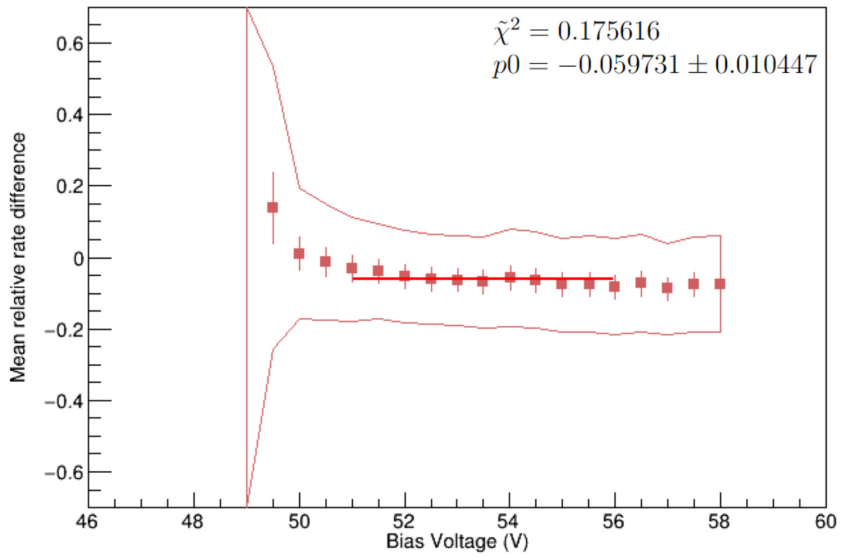

(a) Even rows of sensors S13360-3050VS.

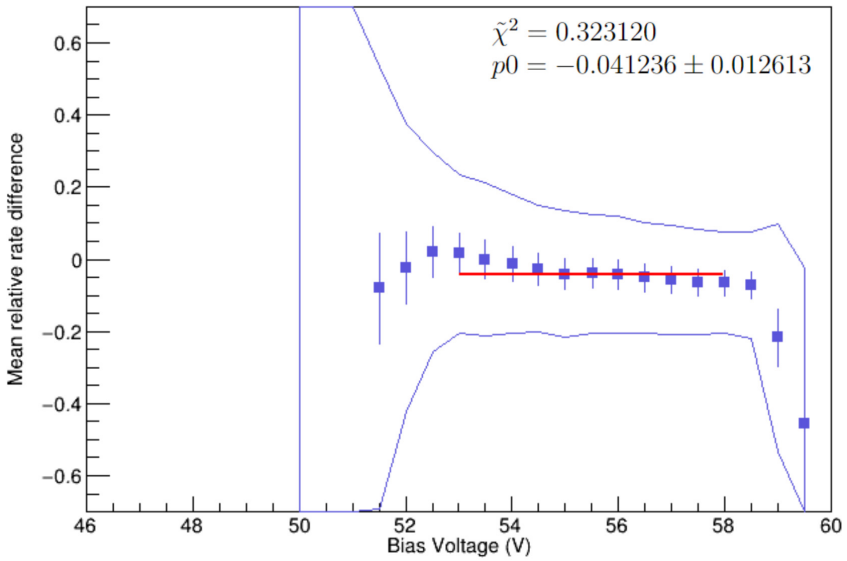

(b) Odd rows of sensors S13360-3025VS.

Figure 3.14: Mean relative rate difference as a function of the bias voltage for even (a) and odd (b) sensors. The plot also shows the fit parameters $p0$, mean relative rate difference, and the $\tilde{\chi}^2 = \frac{\chi^2}{n_{DOF}}$.

3.3 Characterization with flexible PCB

The same measurements of the dark count rate have been collected inside the climatic chamber, set at -30°C, with a prototype flexible printed circuit board (PCB) extension between the HAMAMATSU S13360 and the adapter board. The flexible PCB may allow to keep the electronics on the outside of the box, thus reducing the noise and the dark count rate caused by the power supplied to the parts.

By comparing the measurements taken with and without the flex extension, a difference in the DCR emerged: as shown in Figure 3.15, the DCR is lower in the measurements taken with the flex extension. A probable reason is that by keeping the sensors farther away from the adapter board and the ALCOR, the heat generated from the electronics has a lesser influence on the temperature near the sensors, resulting in a lower dark count rate.

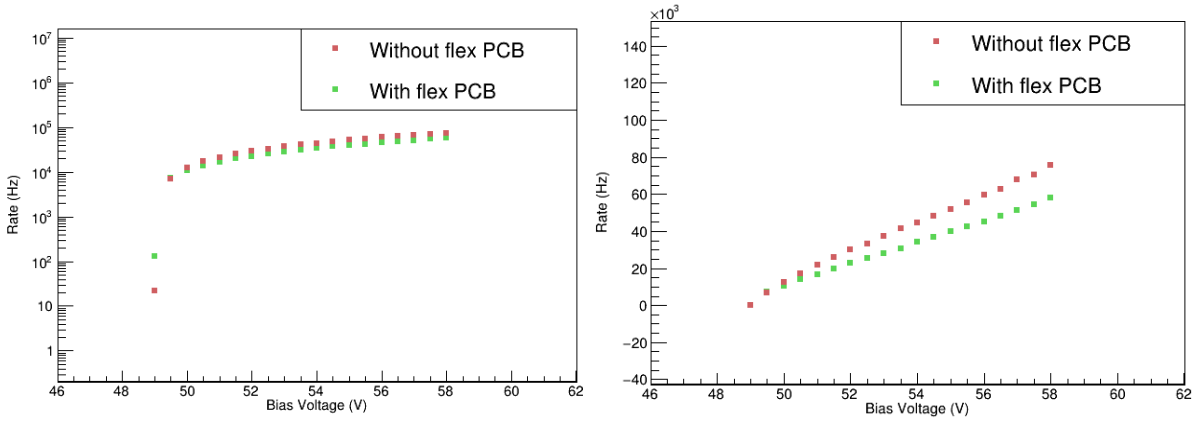

Figure 3.15: Dark count rate as a function of the bias voltage with semi-logarithmic plot (left) and linear plot (right) for one HAMAMATSU S13360-3050VS sensor (channel A1).

Figure 3.16 shows the mean relative rate difference as a function of the bias voltage fit with a constant function for even and odd sensors in the operative range of bias voltage. For both types of sensors, the $\tilde{\chi}^2 = \frac{\chi^2}{n_{DOF}}$ is small enough to assume that the relative difference is constant and does not depend on the bias voltage.

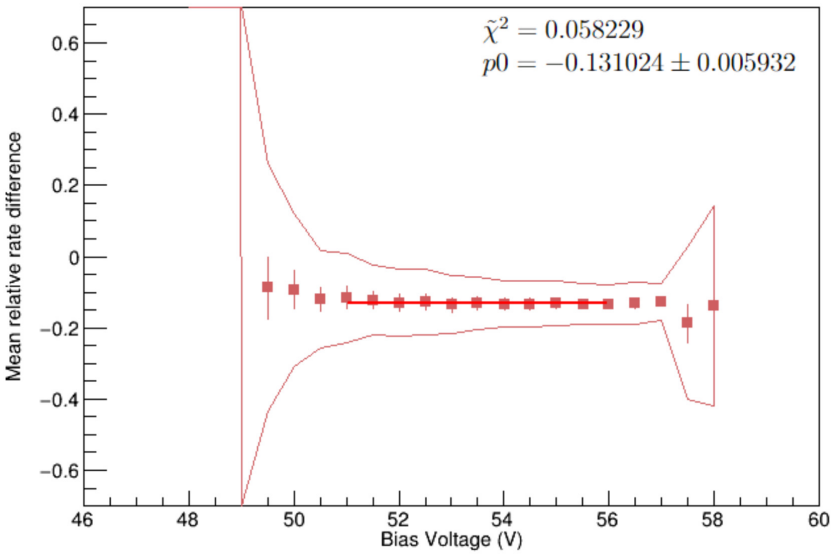

(a) Even rows of sensors S13360-3050VS.

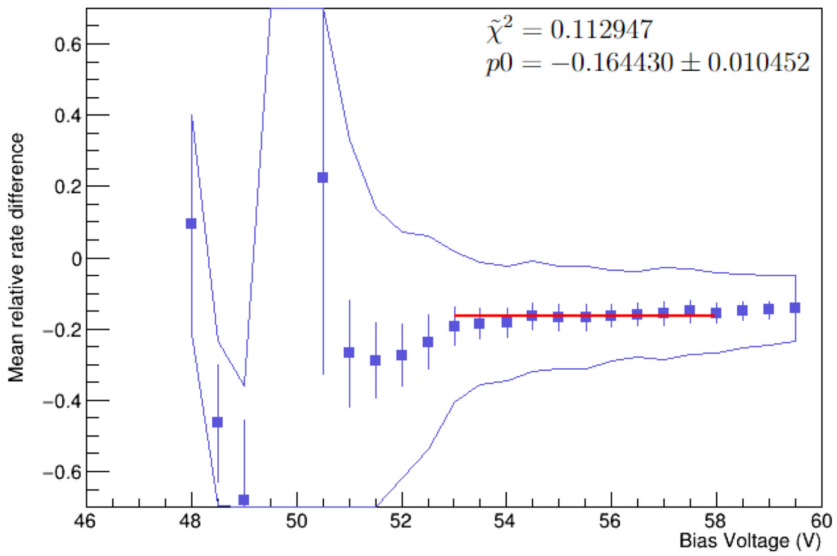

(b) Odd rows of sensors S13360-3025VS.

Figure 3.16: Mean relative rate difference as a function of the bias voltage for even (a) and odd (b) sensors. The plot also shows the fit parameters $p0$, mean relative rate difference, and the $\tilde{\chi}^2 = \frac{\chi^2}{n_{DOF}}$.

Conclusions

The aim of this work was to compare the performance of the prototype readout box with thermoelectric cooling with that of the climatic chamber operating at -30°C.

First, both the cooling system based on the Peltier elements and the climatic chamber were set at -30°C. This resulted in a difference in the dark count rate measured with the two different methods, the one measured in the climatic chamber being unexpectedly higher for all the eight types of SiPM sensors. The plots showing the mean relative rate difference as a function of the bias voltage revealed that the relative rate difference is constant and does not depend on the bias voltage supplied to the boards in the operative range of the sensors.

The difference in the dark count rate observed in the plots brought to attention a difference in the temperature measured by the climatic chamber and the one measured by the sensors mounted on the boards when the surrounding electronics were turned on. By setting the temperature of the climatic chamber to -32.9°C, the temperature on the boards was -30°C while the measurements were taken, resulting in conditions more similar to those inside the prototype readout box. The plots comparing the new measurements taken with the HAMAMATSU S13360 sensors, show a mean relative rate difference of $p0 = -0.06 \pm 0.01$ for the S13360-3050VS sensors and $p0 = -0.04 \pm 0.01$ for the S13360-3025VS sensors. The performance of the thermoelectric cooling system based on the Peltier effect are thus comparable with the performance of the same sensors in the climatic chamber.

Lastly, it was tested the effect of a flexible printable circuit board on the dark count rate. The results show that the DCR is lower than that measured without the flexible PCB under the same conditions. This is believed to be a consequence of the greater distance created by the extension between the sensors and the electronics, resulting in a lower temperature on the board when the flex is present.

Bibliography

[1] A. Accardi et al., "Electron Ion Collider: The Next QCD Frontier - Understanding the glue that binds us all", 2012. https://arxiv.org/pdf/1212.1701.pdf.

[2] R. Abdul Khalek et al., "Science Requirements and Detector Concepts for the Electron-Ion Collider: EIC Yellow Report", 2021. https://arxiv.org/pdf/2103.05419.pdf.

[3] J. Adam et al., "ATHENA detector proposal — a totally hermetic electron nucleus apparatus proposed for IP6 at the Electron-Ion Collider", 2022. https://arxiv.org/pdf/2210.09048.pdf.

[4] R. Alarcon et al., "CORE – a COmpact detectoR for the EIC", 2022. https://arxiv.org/pdf/2209.00496.pdf.

[5] J. K. Adkins, "Design of the ECCE Detector for the Electron Ion Collider", 2022. https://arxiv.org/pdf/2209.02580.pdf.

[6] A. Ghassemi, K. Sato, K. Kobayashi, "A technical guide to silicon photomultipliers (MPPC)", 2021. https://hub.hamamatsu.com/us/en/technical-notes/mppc-sipms.html.

[7] SensL, "An Introduction to the Silicon Photomultiplier". https://elearning.unimib.it/pluginfile.php/521118/mod_folder/content/0/SiPM.pdf

[8] E. Garutti, Yu. Musienko, "Radiation damage of SiPMs", 2018. https://arxiv.org/pdf/1809.06361.pdf.

[9] S. H. Price, "The Peltier Effect and Thermoelectric Cooling", 2007. http://ffden-2.phys.uaf.edu/212_spring2007.web.dir/sedona_price/phys_212_webproj_peltier.html.

[10] "Peltier effect described". https://www.iceqube.com/technical/thermoelectrics-peltier-effect-described/.

[11] Meerstetter Engineering, "Peltier element design guide", 2022. https://www.meerstetter.ch/customer-center/compendium/32-tec-peltier-element-design-guide

[12] R. Kugathasan, "A low-power mixed-signal ASIC for readout of SiPM at cryogenic temperature", 2019. https://pos.sissa.it/370/011/pdf.